A *SPITZER* STUDY OF 21 AND 30 μm EMISSION IN SEVERAL GALACTIC CARBON-RICH PROTOPLANETARY NEBULAE

BRUCE J. HRIVNAK[1], KEVIN VOLK[2], AND SUN KWOK[3,4]

[1] Department of Physics and Astronomy, Valparaiso University, Valparaiso, IN 46383, USA; bruce.hrivnak@valpo.edu
[2] Gemini Observatory, 670 North A'ohoku Place, Hilo, HI 96720, USA; kvolk@gemini.edu
[3] Department of Physics, The University of Hong Kong, Hong Kong, China
[4] Department of Physics & Astronomy, University of Calgary, Calgary, Alberta T2N 1N4, Canada; sunkwok@hku.hk

ABSTRACT

We have carried out mid-infrared spectroscopy of seven Galactic protoplanetary nebulae (PPNs) using the *Spitzer Space Telescope*. They were observed from 10 to 36 μm at relatively high spectral resolution, $R \approx 600$. The sample was chosen because they all gave some evidence in the visible of a carbon-rich chemistry. All seven of the sources show the broad, unidentified 21 μm emission feature; three of them are new detections (IRAS 06530−0213, 07430+1115, and 19477+2401) and the others are observed at higher signal-to-noise ratio than in previous spectra. These have the same shape and central wavelength (20.1 μm) as found in the *Infrared Space Observatory* (*ISO*) spectra of the brighter PPNs. The 30 μm feature was seen in all seven objects. However, it is not resolved into two separate features (26 and 33 μm) as was claimed on the basis of *ISO* spectra, which presumably suffered from the noisy detector bands in this region. All showed the aromatic infrared bands at 11.3, 12.4, and 13.3 μm. Five of these also appear to have the C_2H_2 molecular band at 13.7 μm, one in absorption and four in emission. This is extremely rare, with only one other evolved star, IRC+10216, in which C_2H_2 emission has been observed. Four also possessed a broad, unidentified emission feature at 15.8 μm that may possibly be related to the 21 μm feature. Model fits were made to the spectral energy distributions for these PPNs to determine properties of the detached circumstellar envelopes. The 21 μm feature has been seen in all Galactic carbon-rich PPNs observed, and thus its carrier appears to be a common component of the outflow around these objects.

Key words: circumstellar matter – infrared: stars – planetary nebulae: general – radiative transfer – stars: AGB and post-AGB

Online-only material: color figures

1. INTRODUCTION

The study of infrared emission features in evolved stars provides an important avenue to study the chemistry of the circumstellar environment. First seen in the *IRAS* spectra of four sources (Kwok et al. 1989), a new, broad feature was discovered at ∼21 μm (the so-called 21 μm feature). Subsequently, a small number of additional sources with this feature have been identified based on spectra from *IRAS*, *Infrared Space Observatory* (*ISO*), and with the CGS on the United Kingdom Infrared Telescope (UKIRT). The total number of such sources is about a dozen (Kwok et al. 1999a). An *ISO* study of the strongest sources showed that they all had the same peak wavelength, 20.1 μm, and nearly the same shape with no evidence of substructure (Volk et al. 1999).

The 21 μm sources all possess two characteristics in common. First, the 21 μm sources are all carbon rich. This was first deduced based on the presence of molecular C_2 and C_3 in their visible spectra (Hrivnak & Kwok 1991a; Hrivnak 1995; Bakker et al. 1997) and later confirmed in detailed high-resolution abundance studies (Van Winckel & Reyniers 2000; Reddy et al. 2002). The second common characteristic of the 21 μm sources is that they are nearly all protoplanetary nebulae (PPNs), objects in transition between the asymptotic giant branch (AGB) and planetary nebula (PN) stages of the evolution of intermediate-mass stars. During this stage, the extensive AGB mass loss has ceased and the central star is surrounded by a detached, expanding envelope of molecular gas and dust. This stage can last several thousands of years (Blöcker 1995b), during which the central star evolves from spectral type late-G to early-B, after which time it becomes hot enough to photoionize the gas

and produce a PN (the 21 μm feature also appears to be present but weak in a few young PNs; Hony et al. 2001b; Volk 2003).

There has been an active search for the carrier of the 21 μm feature and many candidates have been suggested, including polycyclic aromatic hydrocarbons (PAHs), fullerenes, and nanodiamonds. Most but not all of the proposed carriers involve carbon. A good match to the feature is produced by TiC (von Helden et al. 2000), but this requires severe formation constraints due to the low abundance of Ti, even in stars like these that have enhanced *s*-process elements. SiC also provides a fit in this region and without the severe abundance constraints (see Speck & Hofmeister 2004 and references therein). However, most carriers suggested have associated emission features at other wavelengths that are absent or unconfirmed in these sources.

A very broad, so-called 30 μm feature has been know for several decades to exist in the spectra of evolved C-rich AGB stars and PNs (Forrest et al. 1981). It has been attributed to MgS (Goebel & Moseley 1985), which peaks in the range of 30–35 μm depending on the temperature of the grain. Subsequent studies have supported this identification (Szczerba et al. 1999; Hony et al. 2002). It has been seen with *ISO* in a number of objects ranging from AGB stars to PPNs to PNs (Hony et al. 2002; Volk et al. 2002) on a dust continuum that peaks at monotonically longer wavelengths in the transition between these stages. On the basis of recent *ISO* spectra, it has been claimed that the feature has been resolved into two features centered at 26 and 33 μm in PPNs, PNs, and extreme-AGB stars (Hrivnak et al. 2000; Volk et al. 2002).

Table 1
Spitzer Observing Log

IRAS ID	LH		SH	
	Date	Time[a]	Date	Time[a]
05113+1347	2006 Mar 17	3 × 14	2004 Oct 03[b]	3 × 30
05341+0852	2007 Apr 16	3 × 14	2004 Mar 22[b]	3 × 30
06530−0213	2006 Apr 25	3 × 14	2006 Apr 25	3 × 30
07430+1115	2007 Apr 27	3 × 14	2007 Apr 27	3 × 30
19477+2401	2005 Oct 16	3 × 6	2004 May 13[b]	3 × 6
22574+6609	2005 Oct 12	3 × 6	2004 Aug 10[b]	4 × 30
23304+6147	2005 Dec 15	3 × 6	2005 Dec 15	3 × 30

Notes.
[a] Number of scan cycles times the on-source integration time in seconds.
[b] Observed in GTO93, PI: D. Cruikshank.

Table 2
Target Positions (2000.0)

IRAS ID	2MASS ID	R.A.	Decl.
05113+1347	05140775+1350282	05:14:07.76	+13:50:28.3
05341+0852	05365506+0854087	05:36:55.06	+08:54:08.7
06530−0230	06553181−0217283	06:55:31.82	−02:17:28.3
07430+1115	07455139+1108196	07:45:51.39	+11:08:19.6
19477+2401	19495491+2408532	19:49:54.91	+24:08:53.3
22574+6609	22591835+6625482	22:59:18.36	+66:25:48.2
23304+6147	23324479+6203491	23:32:44.79	+62:03:49.1

A family of emission features at 3.3, 6.2, 7.7, 11.3, 12.4, and 13.3 μm (historically known as unidentified infrared (UIR) bands) is commonly observed in the diffuse interstellar medium (ISM). Although the specific carriers are not identified, it is quite certain that these arise from the stretching and bending modes of carbonaceous materials with an aromatic component, such as PAHs. We will refer to these as aromatic infrared bands (AIBs). Since these AIBs are also observed in carbon-rich PNs and PPNs, the carriers of these bands are likely to be synthesized in the circumstellar environment of late-type stars. These are often accompanied in PPNs by features at 3.4 and 6.9 μm attributed to aliphatic groups attached to the aromatic hydrocarbons (Hrivnak et al. 2007). The 11.3, 12.4, and 13.3 μm features lie within the wavelength range of the *Spitzer* spectrographs.

In this study, we have obtained *Spitzer* spectra of seven PPNs to further study the 21 μm, 30 μm, and AIB features. These targets were selected with the goal of completing the mid-infrared study of carbon-rich PPNs. In addition to new targets that met this criterion (IRAS 06530−0213, 07430+1115, 19477+2401), we included some carbon-rich PPNs known or suspected to possess the 21 μm feature based on low signal-to-noise ratio (S/N) *ISO* or ground-based spectra. Also included for comparison was one additional object that was well observed with *ISO* but faint enough for *Spitzer* observations.

2. OBSERVATION AND DATA REDUCTION

The target objects were observed with the Infrared Spectrograph (IRS; Houck et al. 2004) on the *Spitzer Space Telescope* (*Spitzer*; Werner et al. 2004). Most were observed as part of program no. 20208, PI: B. Hrivnak. The targets were all relatively bright for *Sptizer* and consequently were all observed in the high-resolution modes, short-high (SH) and long-high (LH). These modes consisted of 10 overlapping orders, and ranged in wavelength from 10–19.6 μm for SH to 19–37 μm for LH. The slit sizes for the two modes are 4″.7 × 11″.3 for SH and 11″.1 × 22″.3 for LH. Each observation consists of two nod positions, located at one-third and two-thirds of the way across the slit; at each nod position three scan cycles were carried out. The spectral resolution is $R \approx 600$. No off-source background measurements were made for these bright targets. An observing log is given in Table 1.

Two of the targets were initially observed using inaccurate coordinates and were re-observed during Director's Discretionary Time. Four of the objects were not observed in this program in the SH mode because they were on the GTO program no. 93, PI: D. Cruikshank. Data for these were obtained from the

Spitzer archive and have been incorporated into this study. Their observations were made in a similar manner to those described above. Details of these additional observations have also been included in Table 1.

Unfortunately, the coordinates of some of the targets were not know accurately and thus the stars were not always centered well on the slits. Accurate positions are important since the slits are relatively small compared to those used in previous mid-infrared spectral observations. In some cases, this meant that the spectrum at one or both of the two nod positions was weak or noisy or could not be extracted properly. Peak up was performed with nearby stars using the Pointing Calibration and Reference Sensor (PCRS). To avoid such problems in follow-up studies, accurate positions are listed in Table 2 for each of the targets as derived from accurate (less than 1″) Two Micron All Sky Survey (2MASS) positions. For the fainter visible sources, source identifications are based on finding charts determined from our ground-based mid-infrared observations. Finding charts for IRAS 19477+2411[5] and 22574+6609 are shown by Hrivnak et al. (1985) and Hrivnak & Kwok (1991b), respectively.

The data were initially processed using the data reduction pipeline at the *Spitzer* Science Center (SSC): version 13.2.0 for the earlier data and version 16.1.0 for the two that were re-observed. We then used the software program SMART (Higdon et al. 2004) to reduce the data. We started with the Basic Calibration Data (BCD) files. These were first cleaned for bad pixels using IRSclean. Bad pixels included the so-called rogue pixels, which are identified by observing campaign at the SSC, and other bad data which are flagged in the pipe line. The spectra were then extracted and defringed. The resulting spectra were examined manually, by order, within each of the individual scan cycles. Bad data were removed from the edges of the orders. Data spikes not present in all the individual scan cycles or in both of the overlap regions in adjacent orders or in both of the nod positions were treated as artifacts, as were some additional large spikes, and these were removed. An average spectrum was composed in each nod position. In some cases, we made small shifts in flux (2%–10%) to bring the overlapping orders into better agreement. The spectra from the two nod positions were then compared and an average spectrum formed if the two spectra agreed. In some cases, as mentioned above, the spectrum from one of the nod positions was near the edge of the slit and the data were of inferior quality; these spectra were not included. The spectral region 14.5–14.6 μm had lots of spikes in the data and was not a region with overlapping orders;

---

[5] Based on comparison with the 2MASS catalog, it appears that the $JHKL'$ magnitudes that we published for IRAS 19477+2401 (Su et al. 2001) were for the nearby source located 8″ west and 5″ south, 2MASS 19495429+2408481. The 2MASS magnitudes for IRAS 19447+2401 are $J = 12.61$, $H = 10.75$, and $K = 9.61$.
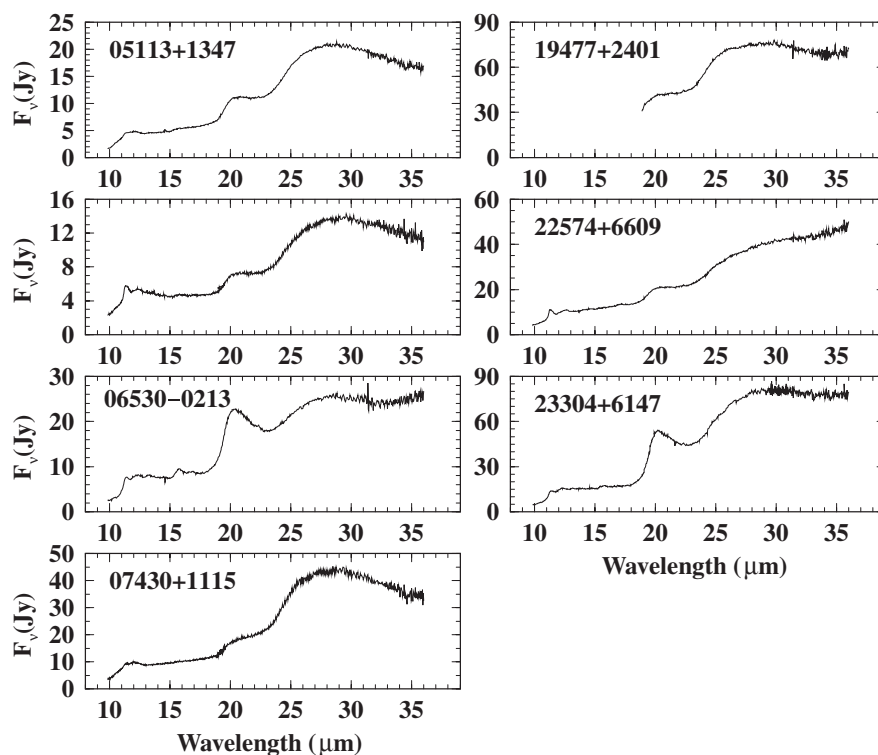
Figure 1. *Spitzer* IRS high-resolution spectra of the seven sources observed with LH. They each display the 21 μm emission feature.

this resulted in particularly noisy spectra in this region. The LH spectra beyond 29 μm were more noisy and those beyond 36 μm were completely deleted.

The SH and LH spectra for each object were then combined, scaling where necessary based on a comparison of the region of spectral overlap from 19.0 to 19.6 μm. In all cases the SH was fainter or similar to the LH; this may be due to the larger slit size of the LH mode, better accommodating small pointing errors. Therefore, we scaled the SH when necessary to match the LH in the overlap region to produce a final *Spitzer* spectrum for reach object covering the region 10–36 μm.

We note for comparison purposes that previous mid-infrared spectra have been obtained of some of the target objects. Initial observations were at low resolution from space with Low Resolution Spectrometer (LRS; 7.7–23 μm, $R \sim 25$) on *IRAS*, or from the air using the Kuiper Airborne Observatory (KAO; 16–48 μm, $R \sim 33$), or from the ground using CGS3 (7.5–13 μm, $R \sim 50$; 16–24 μm, $R \sim 72$) on the 3.8 m UKIRT. Higher-resolution observations were made more recently with SWS01 ($R \sim 250$) or SWS06 ($R \sim 600$–2000) on *ISO*. Some of these will be referenced in our following discussion of the new higher-resolution, higher-S/N *Spitzer* spectra.

3. THE *SPITZER* IRS SPECTRA

IRAS 23304+6147. The SH and LH spectra in the two nod positions were in good agreement and were averaged. In the LH, the longest wavelength order (LH11: 34–36 μm) was scaled upward by 5%. The complete spectrum is shown in Figure 1. The spectrum shows strong broad 21 μm and 30 μm emission features. Also seen are medium-width emission features at 11.4, 12.3, 13.2 μm, a medium-width feature at 15.9 μm, and a weak feature at 22.3 μm. The short-wavelength SH region is shown separately in Figure 2, where the features in that wavelength region can be seen more clearly.
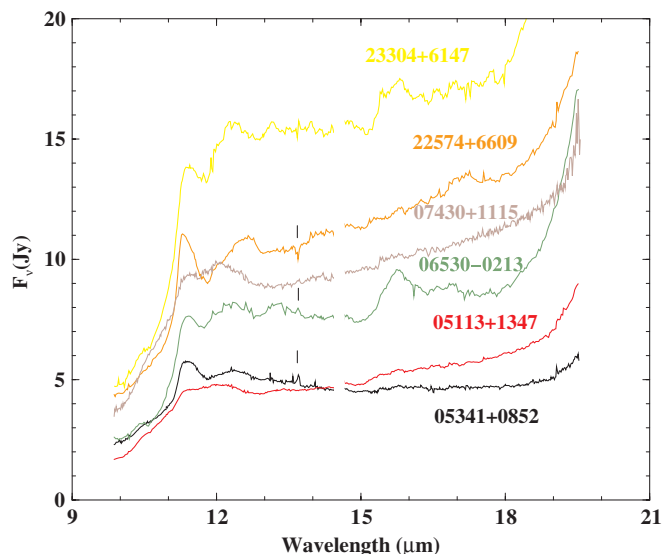

Figure 2. *Spitzer* IRS high-resolution SH spectra of the six sources observed in this mode. They all show AIB emission features. The feature at 13.7 μm (attributed to C_2H_2) seen in three of the spectra is indicated; it may also be present in IRAS 23304+6147 and 07430+1115. (The noisy 14.5–14.6 μm spectral region has been removed from the spectra.)

(A color version of this figure is available in the online journal.)

IRAS 23304+6147 is a well-documented 21 μm source, being one of the original four *IRAS* sources in which this feature was detected (Kwok et al. 1989). The 30 μm feature was discovered by Omont et al. (1995) using the KAO. Good observations were subsequently carried out with *ISO* (Volk et al. 1999; Volk et al. 2002), and we observed it again partly for comparison purposes. Shown in Figure 3 are the *ISO* SWS01 (3–45 μm) and PHOT-S (3–8 μm) and the KAO (16–48 μm) spectra along with the
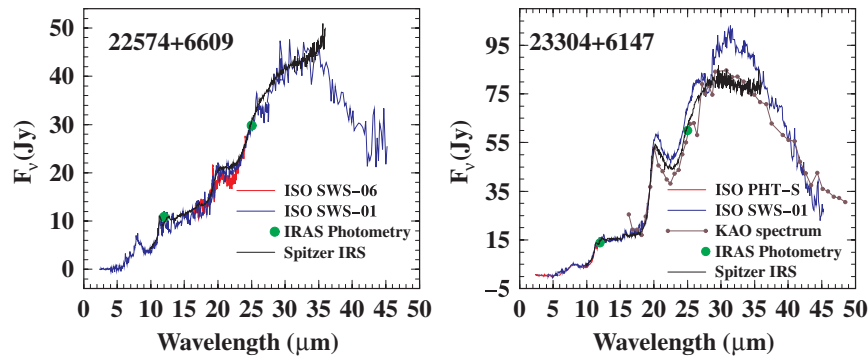
Figure 3. Comparison of *Spitzer*, *ISO*, and KAO spectra of IRAS 22574+6609 and IRAS 23304+6147. The *Spitzer* spectra can be distinguished in the black and white print version by the fact that they extend from 10 to 36 μm for IRAS 23304+6147, the *Spitzer* spectrum lies below the *ISO* spectrum beyond 20 μm.

(A color version of this figure is available in the online journal.)

Spitzer spectrum. It can be seen that the spectra are very similar in intensity from 10 to 19.5 μm and similar in shape from 10 to 27.5 μm. Beyond this, out to 36 μm, the *ISO* spectrum is about 10% higher. The KAO spectrum is roughly similar in flux to the *Spitzer* spectrum beyond 27 μm, but neither it nor the *ISO* spectrum shows the flattening seen in the *Spitzer* spectrum beyond 33 μm. The new *Spitzer* spectrum is noticeably flat between 30 and 35 μm.

The *Spitzer* spectrum was convolved with the *IRAS* bands to calculate synthetic *IRAS* photometry. This resulted in a 25 μm flux of 59.9 Jy, in excellent agreement with the *IRAS* 25 μm flux of 59.1% $\pm$ 4% (53.7 Jy color-corrected). The color-corrected *IRAS* 12 and 25 μm flux measurements have also been included for comparison in Figure 3.

IRAS 05113+1347. The spectra in each of the two nod positions in SH and LH agreed with each other and were averaged. To combine SH and LH smoothly required that we increase the SH spectra by 7%. The spectrum shows a moderately strong 21 μm feature and a strong 30 μm feature. At the shorter wavelengths are seen emission features at 11.4 and 12.1 μm and perhaps weak features at 13.3 and 15.8 μm, along with a weak feature at 22.3 μm.

The 21 μm feature was first detected in this object in a low-S/N CGS3 spectrum from UKIRT following its suggestion in the *IRAS* spectra (Kwok et al. 1995), but the source was not observed with *ISO*. The *Spitzer* synthetic *IRAS* photometry resulted in a 25 μm flux of 14.2 Jy, 7% lower than the *IRAS* 25 μm flux of 15.3% $\pm$ 6% (12.6 Jy color-corrected).

IRAS 05341+0852. The SH and LH spectra in the two nod positions agreed reasonably well with each other and were averaged. The flux levels in most of the SH orders were scaled by a few percent to agree with the adjacent orders, but the data for the first three orders (10–12 μm) agreed well without any shifts. The SH and LH spectra were then combined without any shift in flux. The spectrum shows a strong 11.3 μm feature, a moderately strong 21 μm feature, and a strong 30 μm feature.

The 21 μm feature in this source was also first detected in CGS3 spectra from UKIRT (Kwok et al. 1995); the source was not observed with *ISO*. Present is a feature at 12.4 μm, and a broad but weak feature at $\sim$15.8 μm. Also seen is a very narrow emission feature at 13.7 μm that agrees with the position of the C_2H_2 molecular band seen in absorption in carbon stars. The simulated *IRAS* photometry value was found to be 9.4 Jy at 25 μm, compared to the observed *IRAS* value of 9.9% $\pm$ 7% Jy (8.7 Jy color-corrected).

IRAS 06530−0213. The spectrum was good at only one nod position in each of SH and LH. The longest wavelength order in LH was scaled up by 8% to match the rest of the LH spectrum. The SH spectrum was scaled up by 24% to merge the two spectra; this is presumably to correct for flux missed due to poor centering of the SH spectrum. (Note that if poor centering is indeed the cause of the flux loss, the proper correction is wavelength dependent and not simply a constant scale factor. However, we do not have enough information to make such a correction; thus this likely results in an uncertainty of several percent in the shape of the SH spectrum.) The 21 μm feature is strong; the 30 μm feature is not as relatively strong as in IRAS 23304+6147 and it shows an unusual inflection around 33 μm. Also seen are AIB emission features at 11.4 (strong), 12.3, and 13.2 μm, a strong, medium-width feature at 15.8 μm, and a weak feature at 22.3 μm; the apparent feature at 14.6 μm is likely an artifact. There appears to be a weak, very narrow emission feature at 13.7 μm, the position of the molecular C_2H_2 band.

This object had no previous mid-infrared spectrum, so this is the discovery spectrum of the 21 and 30 μm emission features in this object. The *Spitzer* flux is noticeably lower than the *IRAS* flux, with a synthetic 25 μm flux of 21 Jy as compared with the *IRAS* flux of 27.4% $\pm$ 4% Jy (25.7 Jy color-corrected). This large difference in flux is attributed to flux loss in the *Spitzer* spectrum due to the nonoptimal centering of the object in the slit.

IRAS 07430+1115. In both the SH and LH spectra the two nod positions are in good agreement and were averaged. The SH and LH spectra were combined with no shift in flux, but the very shortest part of the LH spectra was removed due to lack of agreement with the SH in part of the region of overlap. Seen is a 21 μm feature and a strong 30 μm feature. The 11.3 μm feature is seen on a broad plateau extending out to 12 μm. The *Spitzer* flux is close to the *IRAS* flux, with a synthetic 25 μm flux of 27.9 Jy, close to the *IRAS* flux of 29.9% $\pm$ 5% Jy (24.7 Jy color-corrected).

The earlier UKIRT CGS3 spectrum did not reveal the 21 μm feature (Hrivnak & Kwok 1999), but since the CGS3 spectrum only extended to 24 μm and at lower S/N, it is not surprising that this weak feature was not detected. This target was not observed with *ISO*. Thus, this is the discovery spectrum of both the 21 and 30 μm features. Based on the earlier CGS3 spectrum, it had appeared that IRAS 07430+1115 was an exception to the rule that all C-rich PPNs are 21 μm sources. This exception is now removed.

IRAS 19477+2401. Only one of the LH nod positions contained a good spectrum. Neither of the SH nods had a useable spectrum; it was on the edge of the slit and appeared very faint. These problems were traced to poor positioning of the object in our spectrum and misidentification of the source in the SH archival observation. The originally published coordinates were not of sufficient accuracy, but a correct finding chart was shown (Hrivnak et al. 1985). In the one LH spectrum that we used, there was still a need to scale some of the individual orders by a few percent before combining them.

The resulting spectrum is shown in Figure 1. It shows 21 μm feature and a strong 30 μm feature. In addition, there is a weak feature emission at 22.3 μm and possible weak emission features at 28.6, 29.8, 32.6, and perhaps even 34.9 μm. At 31.4 μm there is a narrow dip followed by a narrow peak; since it appeared in two separate orders, we did not remove it from the spectrum. However, it would be quite unusual to see a P Cygni profile at this spectral resolution. The 30 μm feature shows a slight inflection in the spectrum around 33 μm. The synthetic *IRAS* 25 μm flux is 50.5 Jy, 8% less than the *IRAS* value of 54.9% ± 4% (51.2 Jy color-corrected).

IRAS 19477+2401 was observed with CGS3 but the 21 μm feature was not seen in the noisy 20 μm spectrum (Kwok et al. 1995), and the *ISO* spectrum shows flux problems also attributed to an inaccurate position (Hrivnak et al. 2000). This *Spitzer* spectrum is the discovery spectrum for the 21 μm and the 30 μm emission features in this source.

IRAS 22574+6609. In both SH and LH, the spectra in the two nod positions agree well and were averaged. In the LH, we shifted the longest order (LH11) up by 6% to match with the previous order, and the SH was scaled up by 2% to match with the LH. The spectrum shows a moderately strong emission features at 21 μm and 30 μm. A very strong emission feature is seen at 11.3 μm, along with a medium-width feature peaking at 12.6 μm and another one at 17 μm (about 0.5 μm wide). The is evidence of a weak absorption feature at 13.7 μm that may be the molecular band due to C_2H_2.

The 21 μm feature was first detected in this object in the *IRAS* LRS spectrum (Hrivnak & Kwok 1991b), followed by observation of the 21 and 30 μm and AIB features with *ISO* SWS01 (Hrivnak et al. 2000) and SWS06 spectra (Volk et al. 1999, 2002). These previous spectra were rather noisy and the new *Spitzer* spectra show the 21 and 11.3 μm features at much higher S/N. In Figure 3 are compared the *Spitzer* and *ISO* spectra. They have the same general shape out to 35 μm, but the *Spitzer* spectrum is ∼20% higher shortward of 23 μm. The spectral features differ in the region 12–14 μm; the *Spitzer* spectrum shows a feature at 12.6 μm while the noisier *ISO* spectrum shows features at 12.0 and 13.3 μm. The *Spitzer* synthetic 25 μm flux is again less than the *IRAS* flux, 27.3 Jy compared with 29.5% ± 4% Jy (29.8 Jy color-corrected).

We note that in most of the sources (IRAS 06530−0213, 07430+1115, 19477+2401, 22574+6609, 23304+6147) the spectra are flat or even show an upturn in flux beyond ∼33 μm. In the previous spectra of IRAS 23304+6147 and 22574+6609 this was not seen. As mentioned in the discussion of the individual sources, the longest wavelength order, LH11 (34–36 μm), was scaled upward by 5%–8% of some cases to match the rest of the LH spectrum. Although the data are of high S/N, we maintain some skepticism about the accuracy of the shape of the spectra in the 33–36 μm region. Perhaps slit losses make some contribution to the suspected problem, since some of the sources are known to be extended in the *N* band.
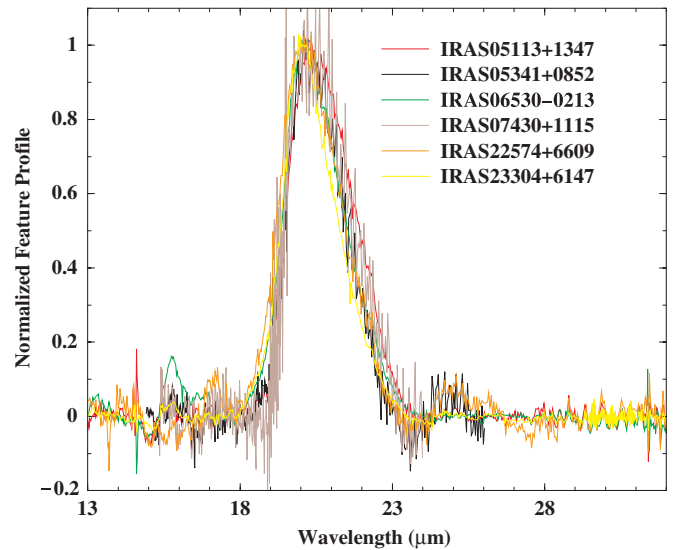

Figure 4. Comparison of the normalized 21 μm spectrum. (Excluded is IRAS 19477+2401 due to the absence of the spectrum shortward of 18 μm with which to set the continuum.)

(A color version of this figure is available in the online journal.)

4. DISCUSSION OF THE SPECTRAL FEATURES

4.1. 21 μm Emission Feature

Volk et al. (1999) used *ISO* spectra to examine the 21 μm feature in eight PPNs, including IRAS 23304+6147 and 22574+6609. They found the feature to have a peak wavelength of 20.1 ± 0.1 μm with a rather similar shape in all eight sources. However, they found a large range in the relative strength of the feature (peak-to-continuum ratio).

We can similarly compare the feature profile in these new, higher-S/N *Spitzer* spectra. This was done for the six objects with spectra in both SH and LH modes (for continuum fitting). To determine the continuum, we used the flux at the shorter and longer wavelength sides and fitted it with a spline function that gave a good smooth fit to this continuum; these ranged in order from 5 to 8. For three of the sources, IRAS 06530−0213, 22574+6609, and 23304+6147, we treated as the continuum the flux at 13–18 μm and at 24–33 μm (which also includes the part of the 30 μm feature), while for the other three, for which there was a more steeply rising continuum on the long-wavelength side, we used a smaller range about the feature. This function was then divided into the spectrum to produce the feature profile. The relative strength of the feature varied quite a bit, from 0.21 to 1.46. An approximately similar range was determined in previous studies of the brighter objects (Volk et al. 1999, 2002; Hrivnak et al. 2000); however these present spectra are superior due to their higher S/N. These peak-to-continuum ratios are listed in Table 3, along with the feature width and peak wavelength for each source. The feature profiles are similar; this is shown graphically in Figure 4, where the profiles have been normalized to 1.000 and the continuum removed. The long-wavelength side of the feature differs slightly among the sources, especially for IRAS 05113+1347. However, this depends sensitively on the 30 μm feature, and the assumption that there is a region of continuum between the two features and thus that the 30 μm feature does not contribute flux between 21 and 24 μm. The short-wavelength side of the 21 μm feature is less susceptible to contamination by strong features and appears to be relatively consistent among the sources. The peak

Table 3
21 μm Feature Profile and Relative Strengths

IRAS ID	Relative Feature Strength	Width (FWZL)[a] (μm)	λ_{peak}[b] (μm)
05113+1347	0.49	5.4	20.2
05341+0852	0.35	5.4	20.1
06530−0230	1.12	6.0	20.1
07430+1115	0.21	4.6	20.2
22574+6609	0.37	5.7	20.1
23304+6147	1.46	5.7	20.1

Notes.
[a] Full width at zero level.
[b] Wavelength of feature peak in a plot of F_ν vs. λ.

wavelength of the feature is 20.1 ± 0.1 μm, the same as found for the sources in the earlier *ISO* study. The feature width we find is greater than in the earlier study, but this is likely due to the fact that we had more continuum to work with. IRAS 23304+6147 was included in both studies, and its 21 μm feature is wider by 20% in the *Spitzer* spectrum.

In all of the 21 μm sources studied in detail, this feature appears to have a relatively similar central wavelength and profile shape in each, but different strengths. Uncertainties arise in defining the feature since it sits upon a continuum and adjacent to a very broad 30 μm feature, both of which are rising steeply toward longer wavelengths.

All carbon-rich PPNs that have been observed possess the 21 μm emission features (Hrivnak et al. 2008). The sole exception to this statement may be IRAS 01005+7910 (B0e). The low-S/N *ISO* spectrum of this source may or may not possess the 21 μm feature; it does possess the 30 μm and AIB features (Hrivnak et al. 2000). Since this is the hottest known carbon-rich PPN and since the feature appears to be absent or weak in PNs, it may be that IRAS 01005+7910 is displaying the expected weakening of this feature with evolution toward a hotter central star. The next hottest carbon-rich PPN star is IRAS 16594−4656 (B7e), and it clearly shows the feature (García-Lario et al. 1999).

The carrier of this feature is still not identified. There have been many suggestions, including PAHs, hydrogenated fullerenes, nanodiamonds, and more recently TiC nanoclusters (von Helden et al. 2000), doped SiC (Speck & Hofmeister 2004; Jiang et al. 2005), and the interaction of Ti atoms with fullerenes (Kimura et al. 2005) (for a review of these and other potential carriers and additional references, see Posch et al. 2004). Some of these predict features at other wavelengths, but none of them have been confirmed. SiC does indeed produce an observed feature at 11.3 μm, but it does not have the correct flux ratio with the 21 μm feature (Jiang et al. 2005). We note below a possibly correlated feature at 15.8 μm in our observed spectra.

4.2. 30 μm Emission Feature: Two Components?

We have previously used *ISO* spectra to study the 30 μm feature in PPNs (Hrivnak et al. 2000; Volk et al. 2002). In these *ISO* spectra it appeared that this very broad feature was resolved into two separate features at 26 and 33 μm, seen with varying strengths in PPNs. These new *Spitzer* spectra do not support this claim. This can be seen by the comparison of the *Spitzer* spectrum with the *ISO* spectrum for IRAS 23304+6147 as shown in Figure 3(b). The apparent downward inflection in the *ISO* spectrum at 27.5–29.5 μm is evidently due completely to the unreliable flux of *ISO* band 3E (27.5–29.5 μm). Also,

the data in *ISO* band 4 (29.5–45 μm) are known to be very noisy due to the many cosmic-ray hits and the flux calibration is less reliable. A similar effect is seen in the comparison of the *Spitzer* spectrum of IRAS 22574+6609 with its *ISO* spectrum as shown in Figure 3(a). The downward inflection in the *ISO* spectrum between 26 and 33 μm is not seen in the *Spitzer* spectrum of IRAS 22574+6609, nor is it seen in any of our other *Spitzer* spectra of sources with the 30 μm feature. Low-resolution *Spitzer* spectra of evolved carbon stars in the LMC also do not show an indication of the 30 μm feature being resolved (Buchanan et al. 2006), although this feature does appear to be significantly weaker in these LMC sources than in similar objects in the Milky Way Galaxy or in these PPNs. Hony et al. (2002) used *ISO* spectra to study the 30 μm feature in a large sample (63) of carbon-rich evolved stars—AGB, post-AGB, and PN. They treated it as a single feature and found that a good fit to the 30 μm profile could be obtained using MgS grains with a temperature differing from the continuum temperature. However, in $\sim$40% of these a residual excess existed at 26 μm. Whether this excess is also an artifact due to the above problems in the *ISO* spectra might be further investigated using *Spitzer* spectra of these *ISO* targets. In a recent paper, Zhukovska & Gail (2008) present a strong case for the feature to be due to MgS as a coating on SiC grains. They go on to show how the feature shape and peak would change with the relative thickness of the coating, with the main peak at 25–28 μm and predicting a subpeak at 33–38 μm when the coating is not too thick.

4.3. AIB Emission Features

A strong 11.3 μm feature is seen along with several corresponding features in the 12–14 μm region and an underlying plateau. The known features at 11.3, 12.1, 12.4, and 13.3 μm are due to out-of-plane bending modes of aromatic compounds with peripheral H atoms attached to the aromatic rings. Although the carriers of these features are frequently attributed to PAH molecules, the strong associated underlying broad continuum suggests that the carrier of the continuum emission cannot arise from small, gas-phase molecules, and has to be emitted by solid-state grains or very large molecules with thousands of C atoms.

To investigate the shapes of these features, we show in Figure 5 the 10–17 μm spectral region with the continuum removed (by division of a fourth-order cubic spline fitted from 10.0–10.5 μm to 14–18 μm). The strong 11.3 μm feature has a relatively consistent peak wavelength of 11.33 ± 0.03 μm (ranges from 11.27 to 11.36 μm in these six PPNs). Shown for comparison is the *ISO* spectrum of IRAS 21282+5050, a young PN with a [WC] central star. Its spectrum in this region has a general similarity to that of the PPNs. However, the 11.3 μm feature is narrower and peaks at a shorter wavelength, 11.21 μm. The peak of the 11.3 μm feature at shorter wavelengths is what is also seen in most other sources. From a sample of 15 objects, consisting of H II regions, young stellar objects, and PNs, Hony et al. (2001a) found that they all had a profile peak very near to 11.23 μm. van Diedenhoven et al. (2004) defined a classification scheme for the 11.3 μm feature that depended upon the shape and peak wavelength of the feature, but all three of their classes (A, AB, B) had peak wavelengths ranging from 11.20 to 11.25 μm. However, Sloan et al. (2007) found in a sample of objects with cooler central stars that the central wavelengths are shifted to the red relative to the above peaks found for the class A and B sources. They include class C AIB features, based on the classification of Peeters et al. (2002),
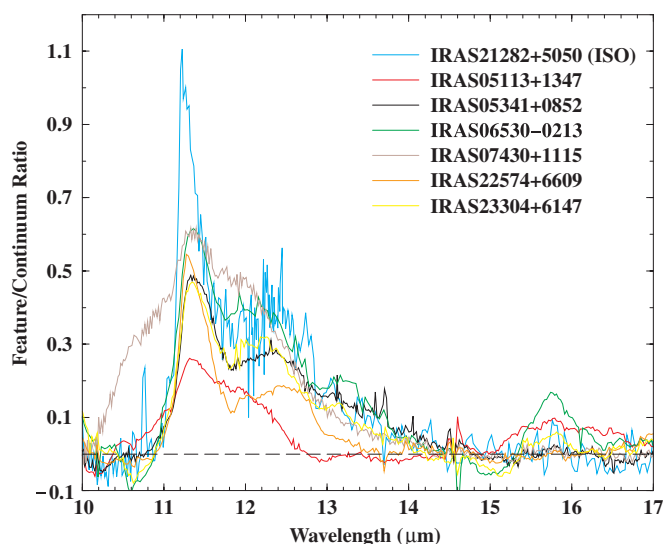
Figure 5. Comparison of the normalized 10–17 μm spectrum for the sources in this study. Included for comparison is the *ISO* spectrum of the young PN IRAS 21282+5050. Seen in all the spectra is the strong emission feature at 11.3 μm; emission at 12.3 μm is seen in most and 13.3 and 15.8 μm in some of them. (The spectra are noisy in the range of 14.5–14.6 μm.)

and these peak at wavelengths similar to what we find. Sloan et al. (2007) attribute the difference in the class C AIB spectra as due to the fact that "the carbonaceous material has not been subject to a strong ultraviolet radiation field, thus allowing the relatively fragile aliphatic materials to survive." Our targets all have cool central stars and aliphatic features (see below), and thus are consistent with this suggestion.

Around 12 μm, a broader emission feature is seen in all of these spectra, with a peak wavelength ranging from 12.0 to 12.6 μm. In IRAS 06530−0213 and 23304+6147 and perhaps 05113+1347, a weaker emission feature is seen at 13.2–13.3 μm. The features at 12.1, 12.4, and 13.3 μm have been identified as the duo, trio, and quatro out-of-plane bending modes of C−H bonds and are associated with the 11.3 μm solo-CH feature (Hudgins & Allamandola 1999). In previous studies of the infrared spectral characteristics of PPNs, we found that unlike PNs and H II regions, PPNs show aliphatic emission features at 3.4 μm (Hrivnak et al. 2007) and 6.9, in addition to the features at 12.1, 12.4, and 13.3 μm which are uncommon in PNs or in other galactic nebulae. This spectral difference is suggested to be the result of chemical evolution, with a progressive formation of larger and larger clusters of aromatic rings and the removal of peripheral aliphatic groups (Kwok et al. 1999b). Absent in these PPNs is the relatively strong, asymmetric 12.7 μm feature found in many objects with AIB features, including IRAS 21282+5050 (Hony et al. 2001a; Sloan et al. 2005, 2007). In this sample, it is found only in IRAS 06530−0213.

The existence of broad plateau emission features at 8 and 12 μm is also a common feature among the PPNs but not PNs and objects with hot central stars (Hony et al. 2001b). This emission plateau is attributed to a collection of out-of-plane bending modes of a miscellaneous mixture of aliphatic side groups attached to the aromatic rings (Kwok et al. 2001). From Figure 5, we can see that the 12 μm plateau feature is present among most of the PPNs observed here, with IRAS 05113+1347 perhaps being an exception. The width of this feature is estimated to be about 2 μm. An exception here is IRAS 07430+1115, which appears to have a broader width extending to 10 μm, although it is hard to set the continuum at the short end of this spectrum.

4.4. 15.8 μm Emission Feature

A relatively strong and medium-wide (∼1.3 μm) feature is seen at 15.8 μm in two of the sources, IRAS 23304+6147 and 06530−0213. The feature also appears to be present but weak in IRAS 05113+1347 and 05341+0852. Moutou et al. (1999) point out features at 15.8 and 16.4 μm in their spectrum of NGC 7023, noting that their widths of ∼0.15 μm are similar to that of the 11.3 μm feature. In the more extensive discussion of sources with features between 15 and 20 μm by Van Kerckhoven et al. (2000), this feature can be seen in two or three sources but is not particularly distinct and is usually weaker than the apparently associated feature at 16.4 μm, which is not present in our spectra. These and the complex of other features which are thought to make up a 15–20 μm emission plateau in carbon-rich sources are attributed to C–C–C bending modes in PAHs. Sellgren et al. (2007) point out additional emission features in NGC 7023 at 17.4 and 17.8 μm, along with a broad plateau feature at 17 μm and a weaker features at 18.9 μm. Our C-rich PPNs show 3.3, 6.2, and 11.3 μm features similar to those seen in NGC 7023 but none of these other, new features. The 15.8 μm features seen in their spectra are not nearly as broad or strong as the 15.8 μm features seen in several of our new PPN spectra, and thus they are not the same.

The width of this feature suggests that it is made up of a larger molecule than that producing the AIB features and perhaps is due to a solid-state feature. To quantify the properties of this feature, we determined it peak wavelength and the relative strength of the feature (peak-to-continuum ratio). For the weaker sources, we determined only an upper limit to the relative strength. The values are as follows: IRAS 06530−0213 (15.75 μm, 0.22), 23304+6147 (15.79 μm, 0.12), 05341+0852 (15.77 μm, 0.06), 05115+1347 (. . . , $\lesssim$0.03), 22574+6609 (. . . , $\lesssim$0.03), and 07430+1115 (. . . , <0.02). In the source with the strongest feature, IRAS 06530−0213, it has a width of 1.3 μm (15.1 to 16.4 μm). The shape in IRAS 23304+6147 is consistent with this and the shape in the weaker sources is also consistent, but the feature in these is of much lower S/N.

As can be seen by comparison with Table 3, the two sources with the much stronger 15.8 μm feature are also the sources in our study with the much stronger 21 μm feature. This raises the possibility of a relationship between these two features. An examination of the lower-S/N *ISO* spectra of other 21 μm sources shows that the 15.8 μm feature is likely present in IRAS 22272+5435, 19500−1709, 16594−4656, 23304+6147 (as confirmed in this *Spitzer* spectrum), and in the low-S/N spectrum of IRAS 07134+1005, the source with the relatively brightest 21 μm feature (Volk et al. 2002; Hrivnak et al. 2000). This possible relationship is based on only a few objects and so is only tentative, but it would certainly be worthwhile to investigate it for more of the 21 μm sources. The presence of a feature correlated with the strength of the 21 μm feature would provide an important clue to help identify the carrier and could at minimum help to constrain the viable suggestions.

4.5. 13.7 μm C$_2$H$_2$ Feature

We have previously mentioned a narrow (unresolved) feature at 13.7 μm in three of these PPNs, in absorption in one (IRAS 22574+6609) and in emission in two (IRAS 05341+0852 and 06530−0213). This is at the wavelength of the molecular C$_2$H$_2$ (acetylene) ν5 band-head feature commonly seen in absorption in carbon stars (Willems 1988; Cernicharo et al. 1999; Volk et al. 2000). This feature may also be present in IRAS 23304+6147

Table 4
Summary of Spectral Emission Features

IRAS ID	SpT	C/O[a]	AIB Features (3–9 μm)[b,c]	Reference[d]	11.3 μm	21 μm	30 μm	13.7 μm[e]	Other Features in *Spitzer* Spectra[b]
05113+1347	G8 Ia	2.4	3.3:, 3.4:	1	Y	Y	Y	N	12.1, 13.3: 15.8(mw):, 22.3
05341+0852	G2 0-Ia	1.6	3.3, 3.4, 6.2, 6.9, 8(br)	1, 2	Y	Y	Y	E	12.4, 15.8(mw)
06530−0213	F5 I	2.8	3.3	1	Y	Y	Y	E	12.3, 13.2, 15.8(mw):, 22.3
07430+1115	G5 0-Ia	· · ·	3.3, 3.4	1	Y	Y	Y	E:	12(mw)
19477+2401	· · · [f]	· · · [f]	· · · [g]	1	· · · [h]	Y	Y	· · · [h]	(no SH spectrum), 22.3, 28.6:, 29.8:, 32.6:
22574+6609	· · · [f]	· · · [f]	· · · [g], 6.2, 6.9, 7.7, 8(br)	1, 2	Y	Y	Y	A	12.6, 17(mw)
23304+6147	G2 Ia	2.8	3.3, 3.4:, 6.2, 6.9, 7.7, 8.6 (8br)	1, 3	Y	Y	Y	A/E:	12.3, 13.2 15.9(mw), 22.3

Notes.
[a] References to C/O abundances: multiple objects—Van Winckel & Reyniers (2000), Reddy et al. (2002); IRAS 06530−0213—Reyniers et al. (2004).
[b] Colons indicate an uncertain detection; mw: medium-wide feature; abs: absorption feature.
[c] Included also are aliphatic infrared bands at 3.4 and 6.9 μm.
[d] References for AIB features: (1) Hrivnak et al. (2007); (2) Hrivnak et al. (2000); (3) review of *ISO* archival spectrum.
[e] E: emission; A: absorption feature; N: no feature.
[f] Faint, with no visible spectra.
[g] Not observed in the 3 μm spectral region.
[h] Not observed in this spectral region with *Spitzer*.

in both absorption and emission (P Cygni profile; see Figure 5) and in IRAS 07430+1115 in emission. This C_2H_2 feature has previously been reported in absorption in only three galactic PPN, AFGL 618 (Cernicharo et al. 2001), AFGL 2688, and IRAS 13416−6243 (Kraemer et al. 2006); it has recently been also seen in absorption in the LMC PPN/PN object SMP LMC 11 (Bernard-Salas et al. 2006) and the SMC PPN object MSX SMC 029 (Kraemer et al. 2006). Kraemer et al. (2006) and Sloan et al. (2007) point out that when the C_2H_2 absorption feature appears in sources with PAH emission, the sources are those classified as the rare class C PAH sources (Peeters et al. 2002). Our sources with C_2H_2 would all be classified as class C PAH sources based on their broad 8 μm features and secondarily based on the longer wavelength of their 11.3 μm feature, and thus this claimed correlation is supported by our new observations.

To our knowledge, C_2H_2 has previously been seen in emission in only one evolved stellar object, the AGB star IRC+10216 (Keady & Ridgway 1993). Thus, this is the first report of the molecule in emission in a post-AGB object. One might consider the emission to be due to collisional excitation. However, collisionally excited H_2 emission is not seen in any of these three PPNs at 2.12 μm (1−0 S(1)) (Kelly & Hrivnak 2005), nor is H_2 emission seen in any objects in this study at 12.27 μm (0−0 S(2)) or 17.03 μm (0−0 S(1)). (Only for IRAS 22574+6609, with a 13.7 μm absorption feature, a (weak) 2.12 μm H_2 emission feature is seen.) We have recently confirmed the presence of C_2H_2 $\nu5$ lines having P Cygni profiles in three of these objects using high-resolution spectroscopy, as will be discussed in more detail elsewhere. This feature has the potential to serve as a diagnostic of the physical conditions in the circumstellar envelope.

4.6. Summary of Spectral Features

We summarize the presence of these spectral features in our targets in Table 4. Also included are the carbon-to-oxygen (C/O) abundance ratio and observations of AIB features at shorter wavelengths as found in other studies. It can be seen that all of the sources in this sample with the 21 μm feature are carbon rich, possess the 30 μm emission feature, and also possess AIB emission features in the 3–14 μm range (except IRAS 19477+2401, which has not been observed in high-S/N spectra in this range). These spectral features appear to

accompany the presence of the 21 μm feature. All of the sources in this study that have visible spectral types also possess C_2 and in most cases C_3 in absorption. In addition to the, in some cases, strong emission feature at 15.8 μm, there is an unidentified weak feature seen at 22.3 μm in four of these sources.

5. MODELING OF THE SEDS

To learn more about the physical conditions under which these features arise (T, ρ), and also to determine the mass-loss rates ($\dot{M}$) and expansion timescales ($t_{\rm dyn}$), we carried out modeling of the circumstellar envelopes. Model fits to the spectral energy distributions (SEDs) were carried out for the six sources with complete 10–36 μm spectra. The continuum was assumed to be due to amorphous carbon (AC) grains, with optical constants by Rouleau & Martin (1991, type AC2) and an assumed size of 0.1 μm. The radiation transfer code by Leung (1976), DUSTCD, was used to produce one-dimensional models. The dust envelope is assumed to have an inner radius $r_{\rm in}$, a dust density profile of $1/r^\alpha$, and to extend to 0.75 pc (somewhat arbitrarily set at the distance reached in 5×10^4 years with an expansion rate of 15 km s^{-1}). The temperature of the central star (T_*) was initially set at the value derived in published atmospheric model analyses and then adjusted slightly ($\leqslant$250 K) to fit the SED at shorter wavelengths. A Kurucz model atmosphere (Kurucz 1993) with log $g = 1.0$ was used for the central star, and this was the assumed energy source for the nebula. The interstellar extinction $A_{\rm V}$ was treated as an adjustable parameter. The other parameters that were initially adjusted were the temperature ($T_{\rm d}$) and inner radius of the cool dust shell, the optical depth ($\tau_{\rm o}$), and the exponent of the density law (α). These were adjusted by trial-and-error fits of the calculated to the observed SEDs until a "best fit" was determined. We began by fitting the mid-infrared continuum at 18 μm and 100 and/or 60 μm; we set $T_{\rm d}$ to the highest value that did not go above the continuum and adjusted $r_{\rm in}$ and α. We then adjusted the optical depth in the near-infrared, along with $A_{\rm V}$ and T_*, to fit the near-infrared and also the visible as well as possible. These parameters are not strongly coupled, with each primarily effecting a distinct aspect of the SED. More details of the basic model are given by Hrivnak et al. (2000).

After initial attempts with this basic model to fit the SEDs of these PPNs, the model was adjusted in two ways. First, in some cases it was found that a single dust shell with the high density

needed to fit the mid-infrared SED and a large radial extent produced flux that was too high to fit the long-wavelength 60 and 100 μm *IRAS* fluxes, even if we assumed a very steep density law ($\alpha \geqslant 4$). Thus we added to the model a discreet thin, dense, cool (c) dust shell of inner and outer radius $r_{in}(c)$ and $r_{out}(c)$, respectively. Second, it was found that for most of the sources the model produced flux that was too low to fit the observations in the *M* and *L* bands. To improve this fit, a component of hot dust was added where needed. This hot (h) component was of low density and mass, and served to bring the model into better agreement with the observed flux in the 3–5 μm region. The hot dust component begins close to the star, with a small value for $r_{in}(h)$. The values for $T_d(h)$ and $r_{in}(h)$ were adjusted to fit the *M* and *L* observations. The density laws for both the cool and hot components are assumed to have the same exponent. The resulting density ratio of the cool to the hot component ($\rho(c)/\rho(h)$) ranges among the models from 7700 to 15,000 at a radius of $r_{in}(c)$, and the hot dust contributes only 1.5%–11% of the optical depth at 11.2 μm.

The AIB plateau features were not included in the modeling. They are likely produced by some combination of fluorescence and nonequilibrium heating, which the dust radiative transfer code does not have the capability to include. However, they do not carry a large part of the total energy emitted in the mid-infrared and presumably therefore would not have much of an effect on the optical depth in the dust shell or the derived parameters. IRAS 22574+6609 is a possible exception to this generalization since it has an unusually high optical depth dust shell.

Empirical fits to the 21 and 30 μm features were added to the continuum. The 21 μm feature template is the same one we used previously to fit *ISO* spectra, derived from the *ISO* high-resolution SWS06 spectra of carbon-rich PPNs. The 30 μm feature template is derived from the fitting of the IRS spectrum for IRAS 05113+1347, since this source has a strong and relatively well defined 30 μm feature. The long-wavelength end of the feature was defined by a linear extrapolation of the observed feature shape from 32 to 36 μm, which goes to zero at 43 μm; that is reasonably consistent with the *ISO* long-wavelength limit of the feature in PPN (Volk et al. 2002; Hony et al. 2002). (The extent to which this template fits or does not fit for the other objects is either telling us something about problems in the IRS data at long wavelengths or is indicating that there are variations in the feature shape.) We did not attempt to empirically fit the AIB plateau features.

These model results are listed in Table 5 and the fits are shown in Figure 6. In calculating the mass-loss rate, a gas-to-dust density ratio of 330 was assumed. Note that while the total mass of the enhanced shell is well determined, the mass-loss rate is less so, since a similar model fit could probably be obtained using a narrower or wider shell of the same mass. Below we briefly discuss the model for each object separately.

IRAS 05113+1347. The fit to the SED of this object required a discrete cool shell. Initial attempts to fit it with an extended dust shell required a very high density exponent of $\alpha = 5$, and even then the fit was not as good as with a discrete shell. The hot dust component is needed to fit the *M*-band flux. This hot component is of low mass, and contributes only 3% of the optical depth at 11.2 μm. The model provides a good fit to the SED, except for the emission plateau from 8 to 14 μm and the 15.8 μm emission feature which were not included in the modeling. The visible image shows only the star, suggesting that we may be looking pole-on to the nebula (Ueta et al. 2000).

IRAS 05341+0852. The SED of this object was fitted by an extended, detached cool dust shell with a high density exponent of $\alpha = 3.5$. To fit the *L* and *M* fluxes, a hot dust component is also needed. This hot component contributes 11% of the optical depth at 11.2 μm but less than 0.03% of the total mass in the envelope. The model fit to the SED is good, except for the emission plateau from 8 to 14 μm and some excess emission observed from 30 to 36 μm. The hot dust component leads to a particularly good fit to the *L* and *M* fluxes. The visible image (Ueta et al. 2000) shows an elongated elliptical nebula around the central star and suggests that one is looking at a bipolar nebula at some intermediate orientation.

IRAS 06530−0213. The SED of this object can be fitted by a normal, detached and extended cool dust shell with no extra hot dust component. The emission plateau from 8 to 14 μm and the strong 15.8 μm emission feature were not fitted. The visible image (Ueta et al. 2000) suggests that one is looking at a bipolar nebula at some intermediate orientation.

IRAS 07430+1115. The modeling of the SED of this object was more difficult than most. An adjustment of the density exponent to its best value resulted in $\alpha = 1$, implying a decreasing mass-loss rate. This is both unlikely and contrary to the results for the others, so we chose to fix $\alpha = 2$, implying a constant mass-loss rate. The resulting model fit was only slightly inferior to that with $\alpha = 1$. The SED was fitted with a low-density envelope and a high-density cool shell region. The observational excess in the *L* band suggests the presence of a hot component for this object also, but without an *M*-band observation, it is too unconstrained to model. The model fit is not as good as most of the other sources. The visible and near-infrared photometry cannot be fitted by a normal model atmosphere with reddening; the resulting compromise fit includes more uncertainty in A_V than in most of the models. The model fit falls below the observations at 60 μm, is not good on the long-wavelength side of the 21 μm features, and falls below the *L*-band flux, as mentioned above. Again, some excess emission is observed from 30 to 36 μm and the emission plateau from 8 to 14 μm is not included in the model fit. The visible image (Ueta et al. 2000) shows an approximately circular nebula around the central star.

IRAS 22574+6609. This source is very faint in the visible ($V = 21.3$) and it lacks a visible spectrum, so we assumed a typical PPN stellar temperature of 5500 K. The model requires a much higher optical depth (τ_o) for this object than the others, by a factor of 10−100. The fit of the model to the SED of this object is good from 18 to 28 μm and then from 60 to 100 μm. The emission plateau rises above the continuum from 8 to 18 μm. Beyond 28 μm, the IRS spectrum continues to rise. An attempt to fit the IRS spectrum to 34 μm leads to a very poor fit to the 60 and 100 μm data. Without spectra extending to 45 μm, it is hard to know exactly where the continuum lies. To fit the *K*-, *L*-, and *M*-band data, a hot component was added to the model, which contributes less than 2% of the optical depth at 11.2 μm. While this brings these data into agreement, we are still left with poor agreement at the shorter wavelengths, with extra flux observed below 2.2 μm and through the visible.[6] Such behavior in dust shell models has been seen previously in one-dimensional models of extreme carbon stars including IRC+10216 and AFGL 3068, and it is attributed to a

---

[6]　The near-infrared measurements of IRAS 22574+6609 by Hrivnak & Kwok (1991b) made with a 15″ aperture likely include the nearby (5″ south) source 2MASS 22591874+6625430, which is brighter in *J* but fainter in *H* and *K*.

Table 5
Results of One-Dimensional Model Fits to SEDs

IRAS ID	τ_o (11.22 μm)	τ_o (V)	α	T_* (K)	L_*/D^2 ($L_\odot$ kpc^{-2})	Cool Dust				Hot Dust			$\rho(c)/\rho(h)$[b]	A_V (ISM)
						$T_d(c)$[a] (K)	$r_{in}(c)/D$ (10^{-3} pc kpc^{-1})	$r_{out}(c)/D$ (10^{-3} pc kpc^{-1})	$\dot{M}/VD$ ($\frac{M_\odot\,\mathrm{yr}^{-1}}{\mathrm{kms}^{-1}\mathrm{kpc}^{-1}}$)	$T_d(h)$[a] (K)	$r_{in}(h)/D$ (10^{-3} pc kpc^{-1})	$\dot{M}/VD$ ($\frac{M_\odot\,\mathrm{yr}^{-1}}{\mathrm{kms}^{-1}\mathrm{kpc}^{-1}}$)		
05113+1347	0.0085	1.2	2.0	5500	170	132	4.2	5.4	4.5×10^{-6}	714	0.043	3.4×10^{-10}	12500	2.8
05341+0852	0.0067	0.94	3.5	6500	126	146	2.5	$\cdots$	1.0×10^{-6}	486	0.117	6.7×10^{-9}	15000	3.7
06530−0213	0.0052	0.73	3.0	7000	280	130	5.4	$\cdots$	1.6×10^{-6}	$\cdots$	$\cdots$	$\cdots$	$\cdots$	5.0
07430+1115	0.018	2.5	2.0[c]	5500	187	139	2.8	3.3	1.1×10^{-5}	$\cdots$	$\cdots$	$\cdots$	$\cdots$	1.5
22574+6609	0.39	55	2.0	5500	145	148	1.0	1.6	3.0×10^{-5}	765	0.029	4.9×10^{-9}	7700	3.0[c]
23304+6147	0.030	4.2	2.5	5500	320	122	5.0	6.4	2.0×10^{-5}	609	0.083	1.7×10^{-9}	10000	1.8

Notes.
[a] Dust temperature at r_{in}.
[b] Density ratio at $r_{in}(c)$.
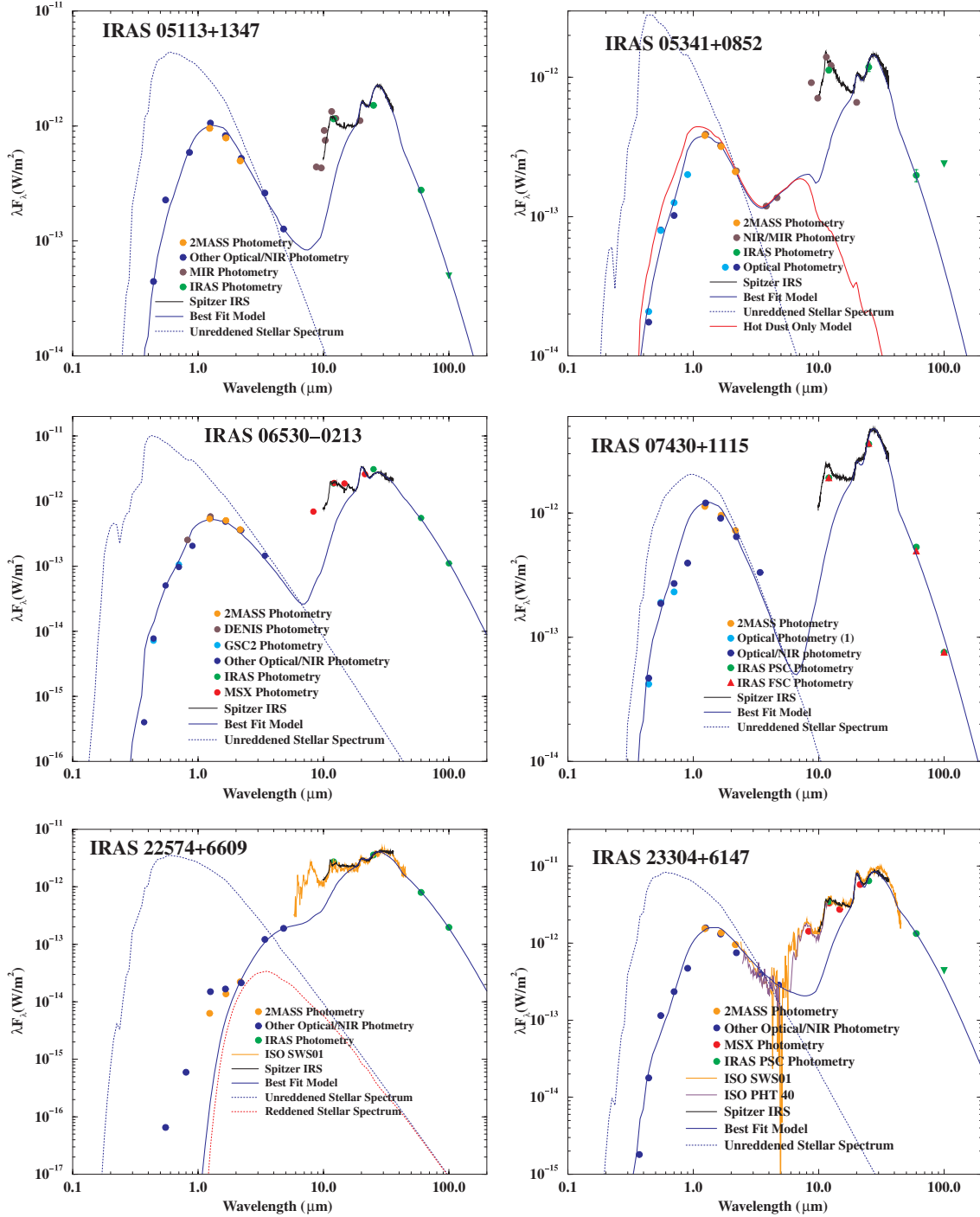[c] Fixed value.

Figure 6. Fits of the models to the SEDs. Included are the ground-based (2MASS, DENIS, NIR: near-IR, MIR: mid-IR, other), *MSX*, *IRAS*, and *ISO* data, in addition to the *Spitzer* IRS spectra.

(A color version of this figure is available in the online journal.)

nonspherical dust shell geometry. This may also be the cause in IRAS 22574+6609. The visible images show a faint, edge-on bipolar nebula with a dark dust lane (Ueta et al. 2000; Su et al. 2001). We suggest that the extra short-wavelength emission is due a low optical depth path (hole) out of the dust shell through which some scattered light is escaping, similar to the situation in IRC+10216 (Men'shchikov et al. 2002). This may be consistent with the off-center intensity peak seen by Sánchez Contreras et al. (2006) in their high-resolution near-IR images of IRAS 22574+6609. They show that this peak is not at the center of the

nebula and thus is not the central star seen directly. We have not tried to add extra complexity to the model simply to fit the visible wavelength portion of the SED. These new model parameters are significantly different from our previous model for this source. However, those were based on much poorer quality *ISO* spectra, in which we chose to disregard the observed *ISO* spectrum from 27 to 45 μm (Hrivnak et al. 2000). The new model was best fit with $A_V = 0.0$; however, galactic extinction studies by Neckel & Klare (1980) suggest a value $\geqslant 2.5$, so we fixed $A_V = 3.0$. The fit was slightly worse, but at a level that is negligible in Figure 6.

IRAS 23304+6147. The model gives a good fit to the SED apart from the emission plateau shortward of 18 μm. A hot dust component is required to fit the *M*-band excess. This hot dust contributes less than 2% of the optical depth at 11.2 μm. The visible image (Sahai et al. 2007) is similar to that of IRAS 06530−0213, and also suggests a bipolar nebula at some intermediate orientation. This new model for IRAS 23304+6147 differs slightly from the one that we previously published based on *ISO* spectra (Volk et al. 2002), due to primarily to the adoption of a stellar model rather than a blackbody for the central star.

Thus it can be seen that the model fits are generally good (excluding the unmodeled AIB emission plateau from 8 to 14 μm), except for IRAS 22574+6609 and perhaps IRAS 07430+1115. Observations in the 5–10 μm range are needed to better constrain the continuum on the short-wavelength side of the AIB emission plateau. Although most of these PPNs are known to have a bipolar morphology, the assumption of spherical symmetry will have little effect on the fitting of the mid-infrared emission and the calculated mass-loss rate. This is the case because the dust shells are optically thin in the infrared where the dust is detected. The only exception to this might be IRAS 22574+6609, where the derived optical depth is much higher than for the other objects. In this case, the morphology might affect the mid-infrared emission and the resulting observed flux would then depend upon observing orientation.

The cool dust temperatures are similar in these models, with values in the range 120–150 K at the inner radius of the cool dust shell. Including an additional six 21 μm sources modeled earlier based on *ISO* spectra, the full range of $T_d(c)$ is 120–210 K (disregarding the earlier model of IRAS 22574+6609; Hrivnak et al. 2000). The absence of C-rich PPNs with higher values of $T_d(c)$ arises partly from the absence of cooler, spectral type K central stars with smaller detached dust shells, even though there is no bias in detecting these (Volk & Kwok 1989). The absence of lower values of $T_d(c)$ at the inner radius of the 21 μm sources suggests that either the carrier is not excited at these lower dust temperatures or that it is destroyed due to the presence of the harder UV radiation field found when the central star has evolved to high temperatures. The value of $T_d(c)$ observed in a particular source depends sensitively on the rate of evolution of the central star as well as the expansion velocity of the detached shell. The temperatures for the hot dust are in the range ∼500–800 K. The density of the cool dust is ∼8000–15,000 times that of the hot dust.

Many of the values in Table 5 are scaled to the distance (*D*), and the mass-loss rate ($\dot{M}$) is also scaled to the expansion velocity (*V*). Assuming a luminosity of 8300 $L_\odot$, appropriate for a core mass of 0.63 $M_\odot$ (Blöcker 1995a) and published expansion velocities, the distances and mass-loss rates for each object were calculated. These are listed in Table 6. The mass-loss rates range from a 10^{-4} $M_\odot$ yr^{-1} to as high as a 6 × 10^{-3} $M_\odot$ yr^{-1}. These later values are very high and cannot be sustained very long in intermediate- and low-mass stars. The total mass of the cool dust shells (ΔM) range from 0.22 to 0.95 $M_\odot$. The total mass of the enhanced shell is a more robust value than the mass-loss rate since the width of the shell is not tightly constrained. The duration of the intense mass loss was calculated based on the shell radii and the expansion velocity, and ranges from 160 to 820 years; again, these values, based on the width of the shell, are not tightly constrained. Thus, the results of the model fits to the SEDs imply that these post-AGB objects lose most of their ejected mass in a short duration of time, 10^2-10^3 years.

Table 6
Model Results for Mass-Loss Rates, Shell Masses, Ejection Durations, and Kinematical Ages

IRAS ID	D^a (kpc)	V^b (km s^{-1})	$\dot{M}$ ($M_\odot$ yr^{-1})	$r_{in}(c)$ (pc)	ΔM ($M_\odot$)	$t(\Delta M)^c$ (yr)	$t_{kin}{}^d$ (yr)
05113+1347	7.0	10	3.2×10^{-4}	0.030	0.25	820	2900
05341+0852	8.2	12	1.0×10^{-4}	0.020	0.27	⋯	1600
06530−0230	5.4	14	1.2×10^{-4}	0.030	0.22	⋯	2100
07430+1115	6.7	15	1.1×10^{-3}	0.019	0.27	180	1200
22574+6609	7.6	26	5.8×10^{-3}	0.008	0.95	160	280
23304+6147	5.1	12	1.2×10^{-3}	0.025	0.66	580	2000

Notes.
[a] Distance based upon assumed luminosity of 8300 $L_\odot$.
[b] Expansion velocities as found in the literature and averaged in some cases.
[c] Duration of enhanced mass loss, determined from $(r_{out}(c) - r_{in}(c))/43V$.
[d] Kinematical age, determined from $r_{in}(c)/V$.

A kinematical age since the end of the high mass-loss phase was calculated based on the inner radius of the cool dust shell and the expansion velocity; this ranges from 1000 to 3000 years for five of the objects but is only 300 years for IRAS 22574+6609. These values are consistent with the evolutionary ages for post-AGB stars Blöcker (1995b). The results suggest that IRAS 22574+6609 may be more massive than the other sources, based on its larger value of the ejected mass, the larger expansion velocity, and the apparently shorter timescale of evolution. The kinematical ages also provide a timescale for the formation of the carrier of the 21 μm feature.

These new results for the mass-loss rate and mass of the ejected shell can be compared with other published values determined in other ways. Here, we have confined ourselves to two different approaches that also involve either discrete denser inner shells or steep density laws.

Ueta and Meixner have recently modeled the mid-infrared emission from the dusty envelopes of two carbon-rich PPNs based on high-resolution images. They used a model that had an extended AGB envelope combined with an equatorially enhanced discrete shell ejected during a later superwind phase. Both of these are sources with 21 μm emission, although they are among the brighter ones and were not included in our present study. For IRAS 22272+5435, the values determined were $\dot{M} = 4 \times 10^{-6} M_\odot$ yr^{-1} and $\Delta t = 1500$ years (Ueta et al. 2001). For IRAS 07134+1005 (HD 56126), for which their model was based on CO interferometric observations in addition to mid-infrared images, they determined $\dot{M} = 3 \times 10^{-5} M_\odot$ yr^{-1} and $\Delta t = 840$ years (Meixner et al. 2004). These mass-loss rate values are a factor of 10–100 lower than what we have determined here.

Hrivnak & Bieging (2005) determined mass-loss rates and shell masses based on their measurements of CO gas in several transitional states, which allowed them to sample the CO emission further out and closer in to the star. The observations were modeled with a one-dimensional statistical equilibrium, radiative transfer code. They did not use a discrete shell with inner and outer boundaries, as we have done here, but they did use a steep density law ($\alpha=3$), which produces a dense inner shell. Their values for the mass loss range from a few × $10^{-4} M_\odot$ yr^{-1} to a few × 10^{-5} $M_\odot$ yr^{-1}, a factor of 10 less than we find here. For three objects in common, our values for the mass-loss rate are larger by factors of 2–100.

A comparison of our new model results for mass-loss rates with two different studies reveals that our rates are a few to 100 times larger, but are confined to a thinner shell. As mentioned above, our mass-loss rates are not as certain as we would like

because the shell widths are not well constrained and assumed to be thin. Similar model fits could likely be produced with somewhat thicker shells with approximately the same total mass. Future higher-resolution (0″.1) imaging that is presently available in the mid-infrared will better constrain these shell widths. It is the total mass that is the better determined parameter from our models. Indeed, comparing the dust masses determined in these studies with our values of 0.7–2.8 × 10^{-3} $M_\odot$ (ΔM/330 from Table 6), one finds much better agreement. Meixner et al. determined a similar value of 0.8 × 10^{-3} $M_\odot$ for IRAS 07134+1005, while Ueta et al. determined a value 20 times smaller, 0.03 × 10^{-3} $M_\odot$ for IRAS 22272+5435. If we compare with the Hrivnak & Bieging (2005) mass-loss values based on CO gas and adjust with our gas-to-dust ratio of 330, we find dust masses 2−4 times smaller than ours, 0.24 × 10^{-3} $M_\odot$ and 0.42 × 10^{-3} $M_\odot$ for IRAS 07134+1005 and IRAS 22272+5435, respectively. However, if our gas-to-dust mass ratio is overestimated by a factor of 2−4, then the agreement would be excellent. Note that Meixner et al. determined a gas-to-dust mass ratio of 75 for IRAS 07134+1005.

6. RESULTS AND CONCLUSIONS

Our targets were selected with the goal of completing the sample of carbon-rich PPNs studied with mid-infrared spectroscopy. However, three additional carbon-rich PPNs were identified in the past few years that were not included (Reyniers et al. 2004, 2007). Therefore, the sample of carbon-rich PPNs that have been observed in mid-infrared spectroscopy is complete except for these three objects. Below are listed results based primarily on the targets of this study, supplemented by more general results for the sample.

1. Three new 21 μm sources were discovered: IRAS 06530−0213, 07430+1115, and 19477+2401. This brings to 16 the total of 21 μm sources among the PPNs (Hrivnak et al. 2008). Improved spectra of this feature were obtained for four others.

2. The shape and central wavelength (20.1 ± 0.1 μm) of the 21 μm feature agrees with that found previously for the brighter sources using *ISO* spectra.

3. These spectra do not show the resolution of the 30 μm feature into two features as was claimed based on *ISO* spectra. The suggested separation apparently was caused by a bad detector band in the *ISO* spectra and is not real.

4. The 11.3 μm AIB feature is seen in all of the sources. The feature has a relatively consistent peak wavelength of 11.33 ± 0.03 μm. However, the presence of the features at 12.3 and 13.3 μm and their peak wavelengths and shapes vary among the sources.

5. These results strengthen the correlation between the presence of the 21 μm feature and evidence of carbon-rich nature of the sources. In particular, all of the 21 μm sources are carbon rich (C/O > 1.0), possess molecular carbon absorption features (C_2, C_3), and possess AIB features (Hrivnak et al. 2008).

6. All carbon-rich PPNs that have been observed possess the 21 μm, 30 μm, and AIB emission features. An exception may be IRAS 01005+7910 (B0e), the PPN with the hottest carbon-rich central star, which may or may not possess a weak 21 μm feature. We also note that IRAS 19500−1709 is unusual in possessing the 21 μm (weak) and 30 μm (strong) features but weak or few AIB features (Volk et al. 2002).

7. The 21 μm feature is present in all (but perhaps one) of the Galactic carbon-rich PPNs but is absent or weak in extreme carbon stars and PNs. This suggests that the carrier is a common part of the outflow during the PPN phase and that the radiation field is important to the presence of the feature. This supports the idea that the 21 μm carrier is produced in the extreme mass loss near the end of the AGB phase, is excited during the PPN phase, and is then destroyed in the more extreme UV radiation field of the subsequent PN phase.

8. A narrow feature at 13.7 μm due to C_2H_2 is observed in the spectra of five objects; it is seen in one source in absorption, in three in emission, and possibly one in both emission and absorption. These represent the first observations of C_2H_2 emission in a post-AGB object. C_2H_2 absorption is commonly seen as a strong feature in the preceding AGB stage of stellar evolution. While most may be incorporated into larger molecules in the evolution to PN, at least some are still present in some region around the star in the PPN phase. Studies of C_2H_2 provide a potential diagnostic of the physical conditions in the circumstellar envelope and should be followed up with high-resolution spectroscopy.

9. At ∼15.8 μm, a broad (∼1.3 μm), unidentified emission feature is seen in the *Spitzer* spectra of four sources. This feature also appears to be present in *ISO* spectra of several additional 21 μm sources. It is particularly strong in the two *Spitzer* sources with the relatively strongest 21 μm feature. This suggests a possible correlation between the two features which, if confirmed, could be a valuable aid in the identification of the 21 μm feature.

10. One-dimensional modeling of the SEDs indicates a dense cool (120–150 K) shell of dust around the stars and also low-density hot (500–800 K) dust closer to the star. The mass-loss rates when the shells detached are high, ranging from a 10^{-4} $M_\odot$ yr^{-1} to a 6 × 10^{-3} $M_\odot$ yr^{-1} but the highest rates were not sustained for long. These result in shell masses of 0.2–1.0 $M_\odot$, ejected over intervals of 160–820 years.

11. The results of the modeling of the dust shells imply ages since the termination of extensive mass loss of 1000–3000 years for all of the sources except IRAS 22574+6609. These ages for the expansion of the shell are consistent with the evolutionary ages of low-mass, post-AGB central stars (Blöcker 1995b), as they should be. IRAS 22574+6609 appears to have only relatively recently left the AGB, ∼300 years ago.

REFERENCES

Bakker, E. J., van Dishoeck, E. F., Waters, L. B. F. M., & Schoenmaker, T. 1997, A&A, 323, 469
Bernard-Salas, J., Peeters, E., Sloan, G. C., Cami, J., Guiles, S., & Houck, J. R. 2006, ApJ, 652, L29
Blöcker, T. 1995a, A&A, 297, 755
Blöcker, T. 1995b, A&A, 299, 727
Buchanan, C. L., et al. 2006, AJ, 132, 1890
Cernicharo, J., et al. 1999, ApJ, 526, L41
Cernicharo, J., et al. 2001, ApJ, 546, L123
Forrest, W. J., Houck, J. R., & McCarthy, J. F. 1981, ApJ, 248, 195
García-Lario, P, Manchado, A., Ulla, A., & Manteiga, M. 1999, ApJ, 513, 941
Goebel, J. H., & Moseley, S. H. 1985, ApJ, 290, L35
Higdon, S. J. U., et al. 2004, PASP, 116, 975
Hony, S., Van Kerckhoven, C., Peeters, E., Tielens, A. G. G. M., Hudgins, D. M., & Allamandola, L. J. 2001a, A&A, 370, 1030
Hony, S., Waters, L. B. F. M., & Tielens, A. G. G. M. 2001b, A&A, 378, L41
Hony, S., Waters, L. B. F. M., & Tielens, A. G. G. M. 2002, A&A, 390, 533
Houck, J. R., et al. 2004, ApJS, 154, 18
Hrivnak, B. J. 1995, ApJ, 438, 341
Hrivnak, B. J., & Bieging, J. H. 2005, ApJ, 624, 331
Hrivnak, B. J., Geballe, T. R., & Kwok, S. 2007, ApJ, 662, 1059
Hrivnak, B. J., & Kwok, S. 1991a, ApJ, 371, 631
Hrivnak, B. J., & Kwok, S. 1991b, ApJ, 368, 564
Hrivnak, B. J., & Kwok, S. 1999, ApJ, 513, 869
Hrivnak, B. J., Kwok, S., & Boreiko, R. T. 1985, ApJ, 294, L113
Hrivnak, B. J., Volk, K., Geballe, T. R., & Kwok, S. 2008, in IAU Symp. 251, Organic Matter in Space, ed. S. Kwok & S. A. Sanford (Dordrecht: Kluwer), 213
Hrivnak, B. J., Volk, K., & Kwok, S. 2000, ApJ, 535, 275
Hudgins, D. M., & Allamandola, L. J. 1999, ApJ, 516, L41
Jiang, B. W., Zhang, K., & Li, A. 2005, ApJ, 630, L77
Keady, J. J., & Ridgway, S. T. 1993, ApJ, 406, 199
Kelly, D. M., & Hrivnak, B. J. 2005, ApJ, 629, 1040
Kimura, Y., Nuth, J. A., III, & Ferguson, F. T. 2005, ApJ, 632, L159
Kraemer, K., Sloan, G. C., Bernard-Salas, J., Price, S. D., Egan, M. P., & Wood, P. R. 2006, ApJ, 652, L25
Kurucz, R. L. 1993, ATLAS9 Stellar Atmosphere Programs and 2 km/s Grid, Kurucz CD-ROM No. 13 (Cambridge, MA: Smithsonian Astrophysical Observatory)
Kwok, S., Hrivnak, B. J., & Geballe, T. R. 1995, ApJ, 454, 394
Kwok, S., Volk, K., & Bernath, P. 2001, ApJ, 554, L87
Kwok, S., Volk, K., & Hrivnak, B. J. 1989, ApJ, 345, L51

Kwok, S., Volk, K., & Hrivnak, B. J. 1999a, in IAU Symp. 191, Asymptotic Giant Branch Stars, ed. T. Le Bertre, A. Lèbre, & C. Waelkens (San Francisco, CA: ASP), 297
Kwok, S., Volk, K., & Hrivnak, B. J. 1999b, A&A, 350, L35
Leung, C. M. 1976, ApJ, 209, 75
Men'shchikov, A. B., Hofmann, K.-H., & Weigelt, G. 2002, A&A, 392, 921
Meixner, M., Zalucha, Z., Ueta, T., Fong, D., & Justtanont, K. 2004, ApJ, 614, 371
Moutou, C., Sellgren, K., L'eger, A., Verstraete, L., & Le Coupanec, P. 1999, in Solid Interstellar Matter: The *ISO* Revolution, ed. L. d'Hendecourt, C. Joblin, & A. Jones (Berlin: Springer), 89
Neckel, Th., & Klare, G. 1980, A&AS, 42, 251
Omont, A., et al. 1995, ApJ, 454, 819
Peeters, E., Hony, S., Van Kerckhoven, C., Tielens, A. G. G. M., Allamandola, L. J., Hudgins, D. M., & Bauschlicher, C. W. 2002, A&A, 390, 1089
Posch, Th., Mutschke, H., & Andersen, A. 2004, ApJ, 616, 1167
Reddy, B. E., Lambert, D. L., Gonzalez, G., & Yong, D. 2002, ApJ, 564, 482
Reyniers, M., Van de Steene, G. C., van Hoof, P. A. M., & Van Winckel, H. 2007, A&A, 471, 247
Reyniers, M., Van Winckel, H., Gallino, R., & Straniero, O. 2004, A&A, 417, 269
Rouleau, F., & Martin, P. G. 1991, ApJ, 377, 526
Sahai, R., Morris, M., Sánchez Contreras, C., & Claussen, M. 2007, AJ, 134, 2200
Sánchez Contreras, C., Le Mignant, D., Sahai, R., Chaffee, F. H., & Morris, M. 2006, in IAU Symp. 234, Planetary Nebulae in our Galaxy and Beyond, ed. M. J. Borlow & R. H. Méndez (Cambridge: Cambridge Univ. Press), 71
Sellgren, K., Uchida, K. I., & Werner, M. W. 2007, ApJ, 659, 1338
Sloan, G. C., et al. 2005, ApJ, 632, 956
Sloan, G. C., et al. 2007, ApJ, 664, 1144
Speck, A. K., & Hofmeister, A. M. 2004, ApJ, 600, 986
Su, K. Y. L., Hrivnak, B. J., & Kwok, S. 2001, AJ, 122, 1525
Szczerba, R., Henning, Th., Volk, K., Kwok, S., & Cox, P. 1999, A&A, 345, L39
Ueta, T., Meixner, M., & Bobrowsky, M. 2000, ApJ, 528, 861
Ueta, T., et al. 2001, ApJ, 557, 831
van Diedenhoven, B., Peeters, , Van Kerckhoven, C. E., Hony, S., Hudgins, D. M., Allamandola, L. J., & Tielens, A. G. G. M. 2004, ApJ, 611, 928
Van Kerckhoven, et al. 2000, A&A, 357, 1013
Van Winckel, H., & Reyniers, M. 2000, A&A, 354, 135
Volk, K. 2003, in IAU Symp. 209, Planetary Nebulae—Their Evolution and Role in the Universe, ed. S. Kwok, M. Dopita, & R. Sutherland (San Francisco, CA: ASP), 281
Volk, K., & Kwok, S. 1989, ApJ, 342, 345
Volk, K., Kwok, S., & Hrivnak, B. J. 1999, ApJ, 516, L99
Volk, K., Kwok, S., Hrivnak, B. J., & Szczerba, R. 2002, ApJ, 567, 412
Volk, K., Xiong, G. Z., & Kwok, S. 2000, ApJ, 530, 408
von Helden, G., et al. 2000, Science, 288, 313
Werner, M., et al. 2004, ApJS, 154, 1
Willems, F. J. 1988, A&A, 203, 51
Zhukovska, S., & Gail, H.-P. 2008, A&A, 486, 229